Chemistry–A European Journal

Research Article
doi.org/10.1002/chem.202401835

Chemistry Europe
European Chemical Societies Publishing

www.chemeurj.org

The Excited State Dynamics of a Mutagenic Guanosine Etheno Adduct Investigated by Femtosecond Fluorescence Spectroscopy and Quantum Mechanical Calculations

Paloma Lizondo-Aranda,[a] Thomas Gustavsson,[b] Lara Martínez-Fernández,[c] Roberto Improta,*[d] and Virginie Lhiaubet-Vallet*[a]

Femtosecond fluorescence upconversion experiments were combined with CASPT2 and time dependent DFT calculations to characterize the excited state dynamics of the mutagenic etheno adduct 1,N^2-etheno-2′-deoxyguanosine (εdG). This endogenously formed lesion is attracting great interest because of its ubiquity in human tissues and its highly mutagenic properties. The εdG fluorescence is strongly modified with respect to that of the canonical nucleoside dG, notably by an about 6-fold increase in fluorescence lifetime and quantum yield at neutral pH. In addition, femtosecond fluorescence upconversion experiments reveal the presence of two emission bands with maxima at 335 nm for the shorter-lived and 425 nm for the longer-lived. Quantum mechanical calculations rationalize these findings and provide absorption and fluorescence spectral shapes similar to the experimental ones. Two different bright minima are located on the potential energy surface of the lowest energy singlet excited state. One planar minimum, slightly more stable, is associated with the emission at 335 nm, whereas the other one, with a bent etheno ring, is associated with the red-shifted emission.

Introduction

The effect of UV radiation on the human body is a topic of obvious importance since it is strongly correlated with a series of pathological events including the appearance of skin cancer.[1] The processes involved between the initial absorption of UV light and the final disorder are extremely complex, but it is clear that the direct energy deposition in DNA/RNA macromolecules plays an important role.[1–5] Indeed, the characterization of the UV-excited electronic states of DNA/RNA and their constituents has been the subject of numerous studies over the years.[1–5] Recently, time-resolved spectroscopic techniques have been applied with success to investigate the ultrafast processes triggered in these molecules by UV light.[1–5] Here, one should distinguish between the mechanisms providing natural protection towards UV light and those responsible for photodamage.

Indeed, natural DNA/RNA constituents present a high resistance towards UV light thanks to the presence of highly efficient non-radiative quenching channels.[1–5] This may not be the case for chemically altered constituents, rendering them much more mutagenic although their relative number may be very small.[1,6–13] Among the naturally occurring altered nucleosides, etheno adducts (ε-adducts) are known to be present as background DNA lesions in rodent or human tissues.[14–18] They were first associated with exposure to environmental carcinogens such as vinyl chloride, which is produced in large quantities in the plastics industry and has been correlated to hepatic angiosarcoma occurrence.[19–21] However, ε-adducts have also been found in unexposed populations.[22,23] This ubiquity has further been explained by their formation as a result of the reaction between nucleobases and highly reactive aldehydes produced during inflammation-induced lipid peroxidation.[24] These adducts are characterized by a five-membered exocyclic ring between a nitrogen atom and an exocyclic nitrogen of the purine or pyrimidine core. A total of four etheno lesions have been identified in DNA, they correspond to 1,N^6-ethenoadenine, 3,N^4-ethenocytosine, 1,N^2-ethenoguanine and N^2,3-ethenoguanine. Their presence in DNA sequence represents a threat for genome integrity because they are mutagenic and cause base translation and transversion.[16,25] Actually, etheno derivatives represent relevant markers of oxidative stress and have been proposed as potential biomarkers for cancer risk assessment in humans.[16,25–28]

We recently reported a combined experimental and theoretical study of the ε-adduct 3,N^4-etheno-2′-deoxycytidine (εdC). Using femtosecond fluorescence spectroscopy and high-level

[a] P. Lizondo-Aranda, V. Lhiaubet-Vallet
Instituto Universitario Mixto de Tecnología Química (UPV-CSIC), Universitat Politècnica de Valencia, Consejo Superior de Investigaciones Científicas, Avda de los Naranjos s/n, Valencia 46022, Spain
E-mail: lvirgini@itq.upv.es

[b] T. Gustavsson
Université Paris-Saclay, CEA, LIDYL, 91191 Gif-sur-Yvette, France

[c] L. Martínez-Fernández
Departamento de Química Física de Materiales, Instituto de Química Física Blas Cabrera, IQF-CSIC, Calle Serrano 119, 28006, Madrid, Spain

[d] R. Improta
Istituto di Biostrutture e Bioimmagini, Consiglio Nazionale delle Ricerche, Via De Amicis 95, I-80145 Napoli, Italy
E-mail: roberto.improta@cnr.it

Supporting information for this article is available on the WWW under https://doi.org/10.1002/chem.202401835

quantum chemistry calculations the excited state relaxations were characterized in detail.[13] We established that the addition of the extra etheno ring on 2′-deoxycytosine (dC) alters its photobehavior and results in a 3-fold increase of lifetime and quantum yield of fluorescence emission centered at 325 nm at neutral pH. Quantum mechanical calculations rationalized these experimental data by evidencing the presence of a sizable energy barrier on the emissive lowest energy ππ* state to reach the ethene-like conical intersection that represents the main nonradiative decay pathway to the ground state. Therefore, the presence of εdC in DNA might slow down the highly efficient non-radiative deactivation channels and act as a doorway for undesired DNA photolability.

Another ε-adduct of interest is 1,N^2-etheno-2′-deoxyguanosine (εdG, Figure 1). Its formation proceeds through the addition of two extra carbons between nitrogen at position 1 and the amine substituent at position C2 by the reaction between 2′-deoxyguanosine (dG, Figure 1) and reactive aldehydes, such as chloroacetaldehyde or 2,3-epoxyaldehydes.[29] This lesion, present as background in humans with a level of ca. 3.7 per 10^8 parent dG,[30] was demonstrated to be mutagenic in *Escherichia coli* and in mammalian cells.[16,31,32] In bacteria, G→A transition, G→T and G→C transversion has been reported with frequencies of 2.05, 0.74, and 0.09%, respectively.[16,32] The apparent mutation frequency is increased more than 10-fold (from 0.4 to 4.6%) in Chinese hamster ovary cells when εdG is incorporated in the DNA sequence.[31] As a matter of fact, the misfunctioning of the DNA repair toolbox[31–34] responsible for the mutagenesis of εdG has been related to the structural perturbations caused by the lesion. NMR studies on the duplex 12-mer 5′-d(CGCATεGGAATCC)-3′·5′-d(GGATTCCATGCG)-3′demonstrated the prevention of conventional Watson-Crick hydrogen bonding, changes of conformation about the glycosyl bonds, and destabilization of the Watson-Crick base pairing of the ε-adduct neighboring bases at 5′ side.[35] By contrast with the aforesaid εdG properties in the ground state, its photophysics and role in DNA photostability have been scarcely reported up to now. In a first time, εdG has been considered as "non-fluorescent",[36] but a very weak emission peaking at 410 nm was evidenced 15 years later.[37]

Here, the advances in time-resolved spectroscopy experiments, providing higher spectral resolution and shorter timescales, are exploited to revisit the description of the excited state relaxation dynamics of εdG. The steady-state and femtosecond fluorescence upconversion experiments were complemented by high-level quantum chemistry calculations. The fluorescence quantum yield was found to be 6 times higher and the fluorescence lifetimes were much longer than those of the canonical nucleoside dG. Moreover, the initial fluorescence anisotropy was found to be very low at all wavelengths, much lower than for dG, indicating that the fluorescent state is not directly populated by 267 nm excitation. Interestingly, the femtosecond fluorescence upconversion experiments indicated the presence of two independent emission bands (stemming from two states or two species). These findings were rationalized by quantum mechanical calculations describing the vertical absorption, adiabatic, and emission energies of the lowest excited states together with the potential energy surfaces associated with the two lowest singlet excited states. Two minima were indeed found on the S_1 energy surface: the less stable S_1-min-asym where the C2 atom of the etheno ring is bent, and S_1-min-pla* with a planar geometry.

Results

Steady-State Absorption and Fluorescence Spectroscopy

Steady-state absorption and fluorescence spectra between 220 and 600 nm were registered in PBS 0.1 M, pH 7.4 (Figure 2). The absorption spectrum consists of two bands; a first band peaking at 286 nm and a second stronger band peaking at 227 nm (Table S1). Inspecting the first absorption more closely, some sub-structure can be seen on the short wavelength side, below 275 nm. This is important to keep in mind since the excitation wavelength chosen for the fluorescence studies was 267 nm. The fluorescence spectrum ($\lambda_{exc} = 267$ nm) is much broader and peaks at 410 nm (Figure 2, Table S1). However, a shoulder can be observed at shorter wavelengths, around 330 nm, together with a long wavelength tail extending beyond 600 nm. As it was reasonable to suppose from the extent of conjugation provided by the etheno ring, both absorption and fluorescence are red-shifted with respect to the canonical dG (Table S1). In addition, a fluorescence quantum yield ϕ_F of ca. 6.5×10^{-4}, ie. more than 6 times higher than that of dG (Table S1), was determined.

To better compare the absorption and fluorescence spectra, they were converted to a wavenumber scale (the fluorescence spectrum was scaled by λ^2), see Figure S4. While the width of the first absorption band is $\Delta\nu_{abs} = 5200\ cm^{-1}$, that of the

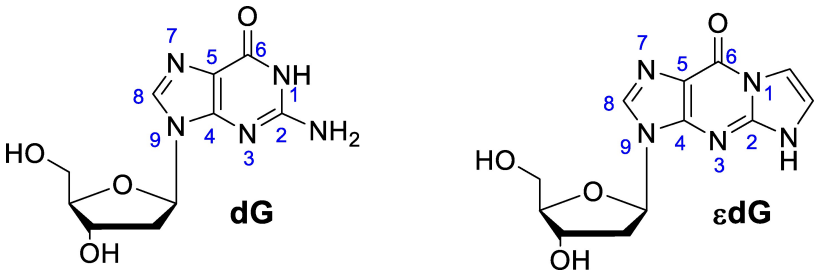

Figure 1. Chemical structure of 2′-deoxyguanosine (dG) 1,N^2-etheno-2′-deoxyguanosine (εdG).

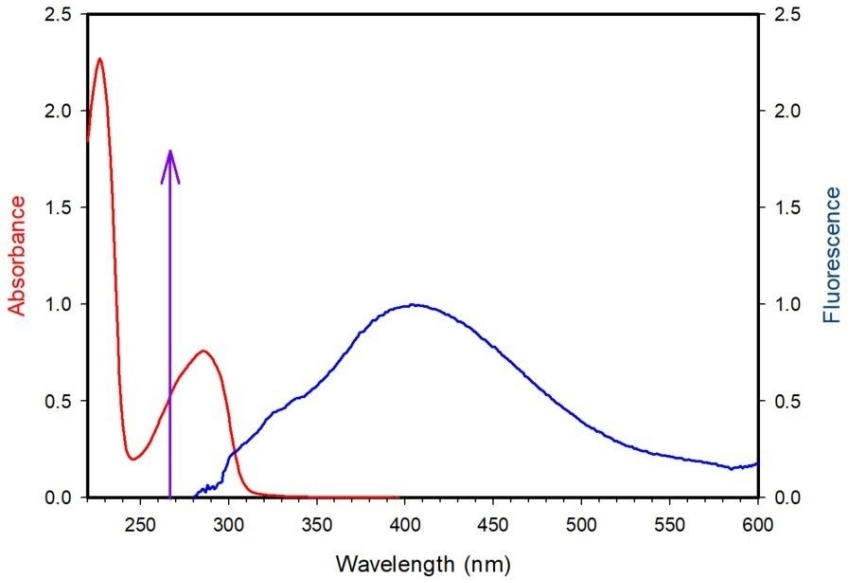

Figure 2. Arbitrary scaled absorption (red) and fluorescence (blue) spectra of εdG in PBS 0.1 M, pH 7.4. The fluorescence spectrum was excited at 267 nm (purple arrow) and corrected for the sensibility of the spectrofluorometer.

fluorescence band is larger, $\Delta\nu_{em} = 8350\ cm^{-1}$. Using the maxima of the absorption and fluorescence bands, the Stokes shift amounts to 11436 cm^{-1}. Interestingly, the second derivative of the absorption band, from 32000 to 40000 cm^{-1}, shows the overlap of two main bands together with some weak sub-bands separated by approximately 1800 cm^{-1}, which might correspond to vibration structures (Figure S5).

Fluorescence Decays

Femtosecond fluorescence upconversion experiments were performed in order to study the time dependence of the emission. Total fluorescence decays of εdG in PBS pH 7.4 (λ_{exc} = 267 nm) recorded at seven different wavelengths over a 10 ps time window are shown in Figure 3a. Complementary decays at three longer wavelengths over a 100 ps time window are shown in Figure 3b. The decays are strongly non-exponential but can be roughly characterized by a fast ps component that dominates at shorter wavelengths ($\lambda < 400$ nm) and a slower component (tens of ps) dominating at longer wavelengths ($\lambda > 400$ nm); an additional small-amplitude constant term is also needed for the fitting at $\lambda > 400$ nm. The fluorescence decays are also represented on a linear scale in Figures S6 and S7. Such a behavior is typical for a fast spectral red-shift, whose origin can be either a continuous displacement or an inhomogeneous shift between two or several overlapping bands. This will be further discussed below when presenting the spectra.

Regarding the fluorescence anisotropy, the situation is also non-trivial. At longer wavelengths (>400 nm), the anisotropy decays over several tens of picoseconds which can be assigned to the rotational diffusion of the molecule. However, a fast rise of a few ps can be observed (Figure 4). At shorter wavelengths (<400 nm), the fluorescence decays are too fast to allow any

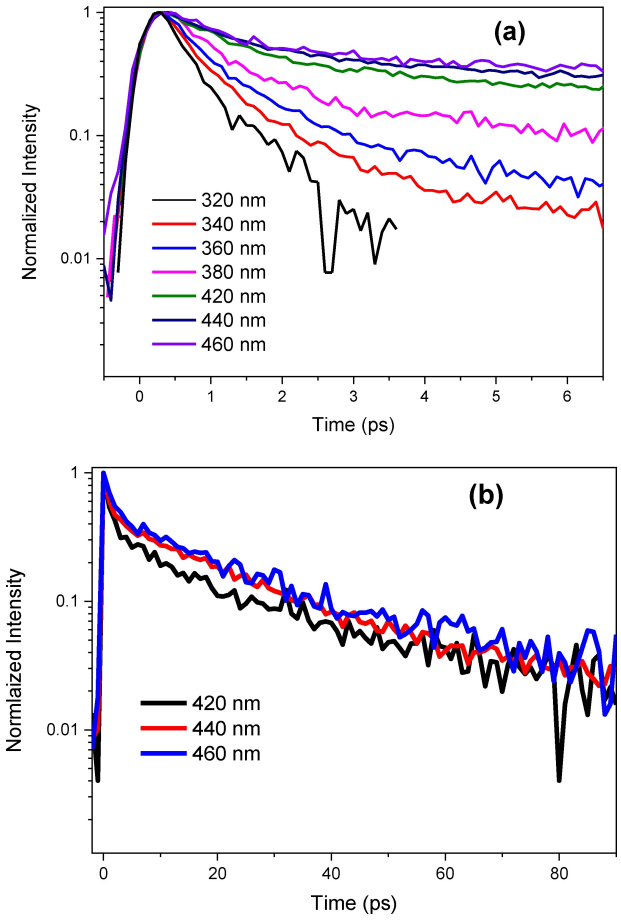

Figure 3. Total fluorescence decays over a time window of 10 ps (a) and 100 ps (b) on a semi-logarithmic scale, obtained from a solution of εdG in PBS pH 7.4 at different emission wavelengths after excitation at λ_{exc} = 267 nm.

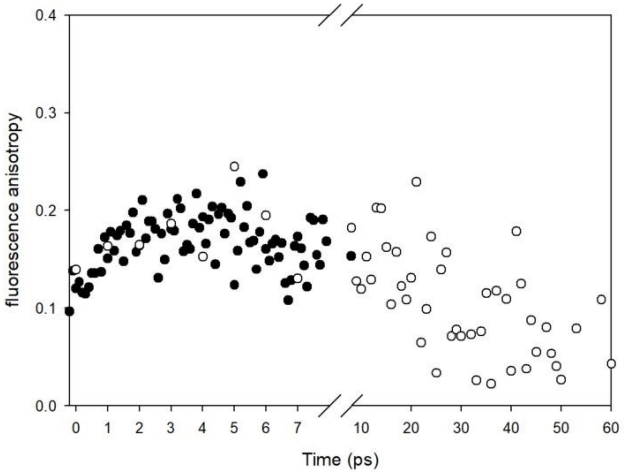

Figure 4. Fluorescence anisotropy decay of εdG in PBS pH 7.4 at 440 nm over a time window of 60 ps. Excitation wavelength $\lambda_{exc} = 267$ nm.

characterization of an anisotropy decay. Interestingly, the fluorescence anisotropy close to zero-time is lower below 400 nm than above, as illustrated in Figure S8. However, the zero-time anisotropy is globally very low, ≈0.1, at all wavelengths. This will be further discussed below.

The actual fitting merged parallel and perpendicular recordings, including both the total fluorescence and the anisotropy in the model description given in the experimental section. The resulting parameters are given in Table 1.

Time-Resolved Fluorescence Spectra

Contour plots of the time-resolved fluorescence of εdG in PBS are shown in Figure 5. The recordings cover the temporal region 0–10 ps, sampled every 1 ps, and the spectral region 310–470 nm, except for a "hole" around 400 nm due to diffused excitation light.

In line with the remarks regarding the fluorescence decays above, it is obvious that an important rapid spectral shift takes place, from a strong band peaking around 335 nm at early times to a weak band centered around 425 nm at longer times.

The time-resolved spectra, together with the kinetics data presented above, allow a better view of the nature of the spectral shift. The spectral evolution is not in consonance with a continuous red-shift of a single band, as in the case of solvation dynamics, but is due to two separate contributions of a strong short-lived 335 nm band and a weak long-lived 425 nm band. Actually, the extraordinarily broad steady-state fluorescence band can be understood as the sum of the 335 and the 425 nm bands. In order to get a clearer picture, the spectra were converted on a wavenumber scale (after scaling by λ^2) as shown in Figure S9.

Fitting the experimental spectra with a simplified lognormal function does not result in a satisfactory fit. Instead, a simple two-band description reproduces the observed data well. As a model two fixed Gaussian functions with adjustable amplitudes were used. The central positions of the two bands were fixed to 29080 cm^{-1} ("blue" band) and 23900 cm^{-1} ("red" band) respectively. The spectral width for both bands was fixed to 2200 cm^{-1}. The resulting fitted model spectra are also shown in Figure S9. The resulting time-evolution of the intensity amplitudes of the two bands is shown below in Figure 6.

As can be seen, the time dependence is very different for the two bands. While the "blue" band drops by about 80% within 1 ps and practically attains the zero level at 5 ps, the intensity of the "red" band decreases much more slowly and remains on the 25% level at 10 ps.

Computed Absorption and Emission Energies

Calculations in the Gas Phase

For quantum mechanical calculations, the effect of the deoxyribose moiety has been mimicked by a methyl group (εG, see Figure 7), which has been previously shown to be able to reproduce the excited state behavior of ethenocytidine[13] and guanine satisfactorily.[38]

In Table 2, we report the Vertical Absorption Energy (VAE) computed for the three lowest energy excited states of εG in the gas phase. Confirming previous indications,[13] the VAE computed at the M052X level are overestimated (by ~0.7 eV) with respect to the CASPT2 values. TD–M052X and CASPT2 agree on the presence of two bright ππ* transitions (HOMO (H)→LUMO (L) and H→L+1) of similar intensities, with an energy gap of 0.3 eV. While these two transitions are the lowest in energy on the CASPT2 level, a nπ* transition appears as the

Table 1. Fitted lifetime components and anisotropies from the fluorescence decays of εdG in PBS, merging short and long timescales.

λ (nm)	320	340	360	380	420	440	460
a_1	0.72 ± 0.04	0.94 ± 0.01	0.90 ± 0.01	0.85 ± 0.01	0.72 ± 0.01	0.66 ± 0.01	0.61 ± 0.01
τ_1	0.21 ± 0.04	0.56 ± 0.02	0.62 ± 0.02	0.66 ± 0.03	0.96 ± 0.03	1.09 ± 0.02	1.06 ± 0.05
a_2	0.28 ± 0.04	0.06 ± 0.01	0.10 ± 0.01	0.15 ± 0.01	0.26 ± 0.01	0.33 ± 0.01	0.37 ± 0.01
τ_2	0.88 ± 0.08	7.5 ± 0.9	6.3 ± 0.5	10.1 ± 1.1	20.4 ± 1.4	24.9 ± 1.0	23.5 ± 1.5
a_3	-	-	-	-	0.022 ± 0.004	0.012 ± 0.003	0.023 ± 0.006
τ_3	-	-	-	-	(constant)	(constant)	(constant)
r_0	0.043 ± 0.004	0.038 ± 0.003	0.053 ± 0.003	0.069 ± 0.004	0.103 ± 0.004	0.116 ± 0.003	0.095 ± 0.006

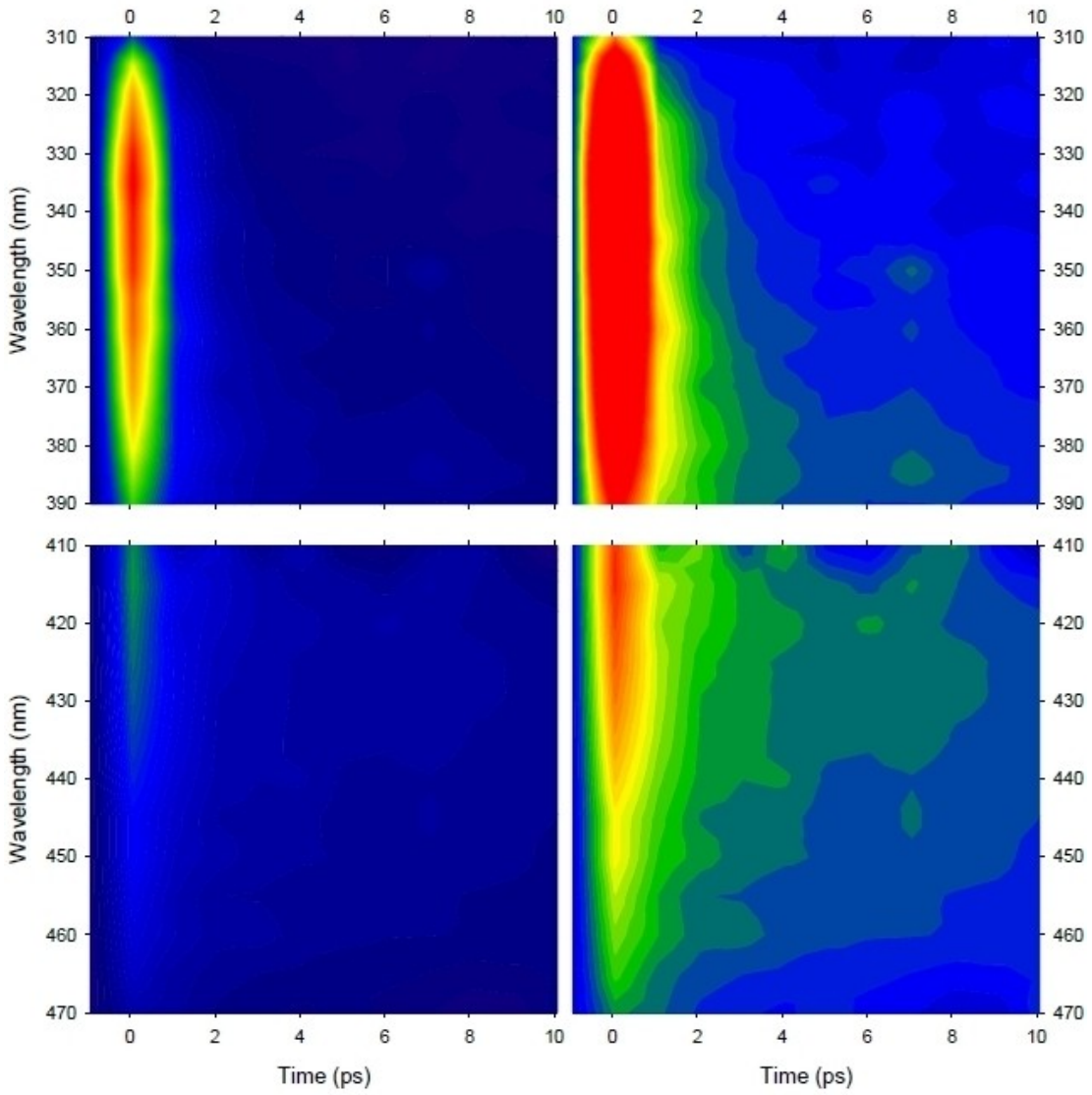

Figure 5. The corrected time-resolved fluorescence of εdG in PBS pH 7.4 as contour plots over a wavelength region {310,470}nm and a time window of 10 ps. The two panels correspond to different intensity scales of the same data. Excitation wavelength $\lambda_{exc} = 267$ nm

Table 2. Vertical Absorption Energies (VAE, in eV) and oscillator strengths (a.u., in parentheses) computed for εG in the gas phase at the M052X the CASPT2 levels.

	M052X/6-31G(d)	CASPT2/6-31G(d)	description
S_1	5.18 (0.14)	4.58(0.18)	ππ* H→L
S_2	5.49 (0.23)[a]	4.88 (0.19)	π* H→L+1
S_3	5.42 (0.00)	5.54 (0.00)	nπ*

[a] At this level corresponds to S_3.

second one at the M052X level. This nπ* transition involves in particular the Lone Pair of the carbonyl oxygen atom.

Geometry optimizations of the ππ* transitions (S_1 and S_3) at the TD–M052X/6-31 G(d) level of theory in the gas phase lead to the same bright minimum of S_1 (adiabatic energy 4.93 eV), characterized by an emission energy of 4.68 eV (i.e. Stokes shift 0.5 eV) and a planar geometry. Contrary, optimization of S_2 (nπ*) ends up in a dark S_1 minimum that is only slightly (0.002 eV) less stable compared to the bright one. A qualitatively similar picture is obtained at the CASSCF/CASPT2 level when optimizing the lowest-lying state. We find a more stable bright minimum with emission energy of 4.0 eV (i.e. with a Stokes Shift of 0.58 eV, considering the energy of the S_1) and adiabatic energy of 4.30 eV, and a dark minimum with adiabatic energy 4.72 eV.

Calculations in Water

In Table 3, we report the VAEs computed for the lowest energy excited states of εG in water, by using two different computational models, i.e. (i) εG, where only bulk solvent effects (PCM)

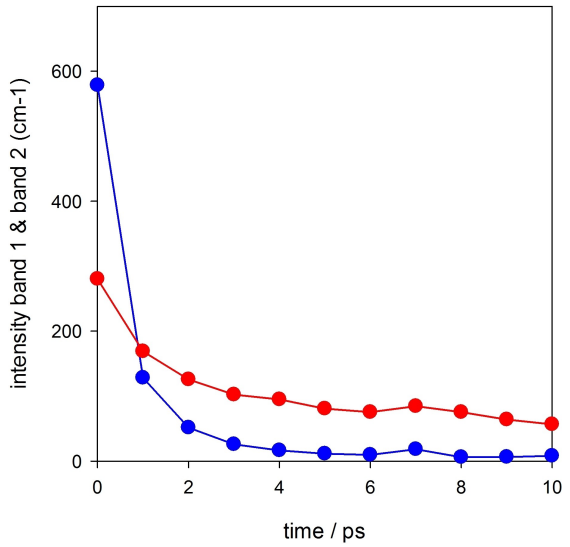

Figure 6. Relative time-dependent intensities for the two Gaussian model functions fixed at (blue) 29080 and (red) 23900 cm^{-1}, respectively.

are included, and (ii) εG•3H_2O (see Figure 7), where, three water molecules of the first solvation shell are also included in the model (see Computational details).

According to M052X, independently of the basis set adopted, the two lowest energy excited states in the Franck-Condon (FC) region, S_1 and S_2, correspond to ππ* transitions. The former is more intense and shows a predominant H→ L contribution, whereas the latter has H→ L+1 character. A schematic drawing of the involved frontier orbitals is reported in Figure S10 of the SI. These two transitions have similar oscillator strengths and, interestingly, their relative intensity is quite sensitive to the size of the basis set, to the inclusion of solvent effects and to the solvation time regime adopted (equilibrium or non-equilibrium, see SI). Indeed (see Table 2) in the gas phase S_2 results more intense than S_1 at the M052X/6-31G(d) level. According to our calculations, the most realistic picture of S_1 and S_2 in the FC region is that of two strongly vibronically coupled excited states, whose interplay (e.g. the relative intensity) is modulated by the intramolecular or intermolecular (solute-solvent) vibrational degrees of freedom. These two transitions are associated with the lower energy absorption band, which indeed exhibits a shoulder at higher energy (Figure 2), which should be due to S_2.

Another bright excited state, much more intense than S_1 and S_2, is present ~1.1 eV higher in energy with respect to the lowest energy absorption band. This excited state is responsible for the second absorption band found around 227 nm in the experimental spectra (Figure 2), more intense than the first one and with a maximum blue-shifted by ~1.3 eV.

In Table 3, we also report the results obtained by using the same computational approach and a similar model (G•5H_2O) for the parent dG base. In this latter molecule, the two lowest energy excited states are also ππ* transitions, which, according to the Platt's nomenclature are usually labelled as L_a and L_b. In dG, L_b transition is more intense and is responsible for the maximum of the absorption band. Our calculations predict that etheno substitution leads to a significant red-shift of the maximum of absorption band of ~0.7 eV, focusing on the most intense transitions. Considering that we are neglecting vibrational contributions (see below) this estimate is fully consistent with the experimental results. We note that for this reason excitation around 267 nm populates preferentially the second excited ^{1}ππ* state (S_2).

When applied to the smaller non-solvated εG model, our calculations provide results like that obtained for εG•3H_2O. The only significant discrepancy concerns the relative intensity of S_1 and S_2, the latter being now the most intense transitions. Overall, the picture of the FC region obtained in water is thus like that found in the gas phase, but for the 'usual' destabilization of the dark nπ* transition.[2,3]

As shown in Figure 8, the computed absorption spectrum is in very good agreement with the experimental one, but for a blue-shift, due to the use of M052X/6-31G(d) calculations. However, when including vibrational effects, the discrepancy

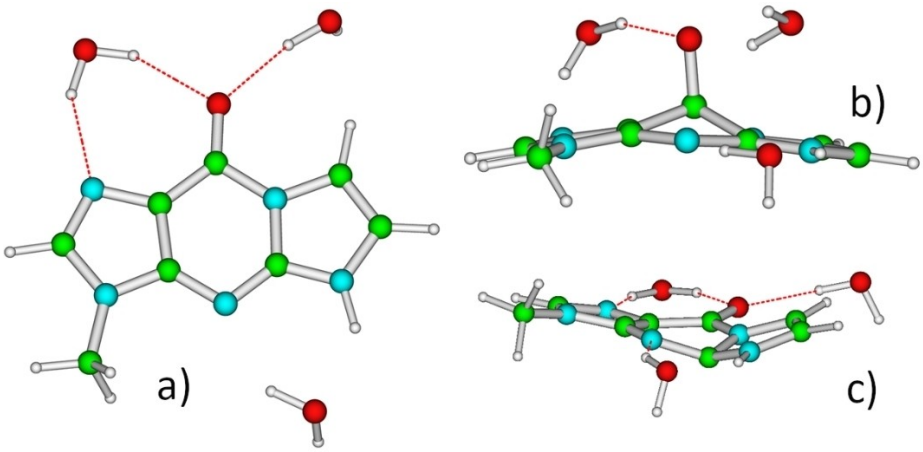

Figure 7. a) Schematic drawing of the εG•3H_2O model, including 3 H_2O molecules of the first solvation shell, and mimicking the sugar with a methyl group. b) εdG structure in the crossing region S_1/S_0, located at the PCM/TD–M052X/6-31G(d) level c) S_1-min-asym minimum located by optimizing S_2 at the PCM/TD–M052X/6-31G(d) level. Color code: carbon atoms (green), oxygen atoms (red), nitrogen atoms (cyan), hydrogen atoms (white).

Table 3. VAE (in eV) and oscillator strengths (a.u., in parentheses) computed for εG•3H$_2$O and εG in water at the PCM/M052X level, using different basis sets, on geometries optimized at the PMC/M052X/6-31G(d) level. For comparison the VAE and oscillator strengths for the canonical base G•5H$_2$O are also given.

	εG•3H$_2$O				G•5H$_2$O	
Excited State	6-31G(d)	6-31+G(d,p)	6-311+G(2d,2p)	Description	6-311+G(2d,2p)	Description
S$_1$	5.03 (0.20)	4.90 (0.24)	4.83 (0.22)	ππ* H→L	4.99 (0.20)	ππ* H→L
S$_2$	5.40 (0.15)	5.31 (0.13)	5.26 (0.10)	ππ* H→L+1	5.53 (0.45)	ππ* H→L+1
S$_3$	5.88 (0.00)	5.93 (0.00)	5.93 (0.00)	nπ*	5.99 (0.0)	nπ*
S$_4$	6.23 (0.90)	6.06 (0.96)[a]	5.99 (0.99)[a]	ππ* H-1→L		
	εG					
S$_1$	5.12 (0.16)	4.99 (0.21)	4.91 (0.19)	ππ* H→L		
S$_2$	5.42 (0.26)	5.31 (0.24)	5.26 (0.20)	ππ* H→L+1		
S$_3$	5.61 (0.03)	5.83 (0.01)	5.70 (0.00)	nπ*		
S$_4$	6.36 (0.80)	6.14 (0.84) [a]	6.06 (0.88)	ππ* H-1→L		

[a] Corresponds to S$_5$.

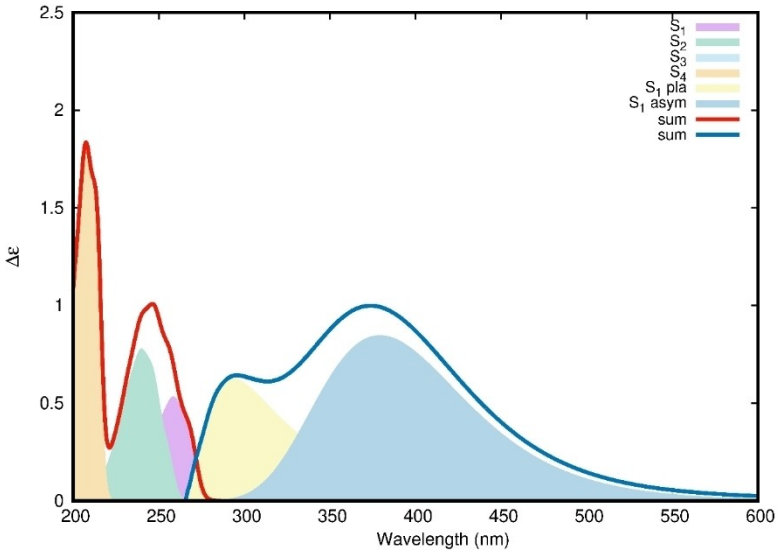

Figure 8. Computed vibrationally resolved absorption and emission spectra for εG obtained by using PCM-TD–M052X/6-31G(d)-FC-classes calculations. The emission spectrum has been simulated by assuming that the population of S$_1$-min-pla* and S$_1$-min-asym are the same. The blue-shifted spectra by respect to experimental ones is due to the use of M052X/6-31G(d) calculations.

with experiments significantly decreases. Based on the average of the VAE of S$_1$ and S$_2$. The absorption maximum would fall at 5.3 eV, the computed absorption maximum in the vibrationally resolved spectrum falls instead at 250 nm (~4.95 eV). This result confirms that vibrational effects strongly modulate the position of the band maxima.[39]

We have then optimized the geometry of the two lowest energy excited $^1\pi\pi^*$ states (S$_1$ and S$_2$) states, by using both the 6-31G(d) and the 6-311+G(2d,2p) basis sets, on both εG•3H$_2$O and εG models. As summarized in Table 4, for εG•3H$_2$O, geometry optimization of S$_1$ leads to a stationary point, with a very low energy gradient (<0.0002 a.u.), where the purine ring keeps a planar geometry (S$_1$-min-pla*), and an emission energy of 4.43 eV (PCM/TD–M052X/6-31G(d) calculations), i.e. with a Stokes shift of ~0.6 eV. This value is one-half of the experimental one, since in the steady-state emission spectrum we observe a broad band peaking at 410 nm, i.e. with a Stokes Shift of ~1.3 eV. However, it is noteworthy that the theoretical value is consistent with the experimental one of 0.63 eV, obtained at 335 nm in the femtosecond fluorescence upconversion experiments. In fact, frequency calculations on S$_1$-min-pla* show the presence of an imaginary frequency of −100 cm^{-1}, associated to the out of plane motion of the carbonyl group, indicating that S$_1$-min-pla* is not a real minimum of the S$_1$ potential

Table 4. Adiabatic energy, oscillator strengths (a.u., in parentheses), and emission energies (italics, red) computed for the different excited state minima of εG•3H_2O at the PCM/TD-M052X level, using different basis sets. Stokes shift with respect to S_1 absorption energies in the FC point are also reported. Energy values in eV.

	6-31G(d)		6-311 + G(2d,2p)	
	S_1	S_2	S_1	S_2
S_1-min-pla*	4.68 (0.32) *4.43*		4.50 (0.36) *4.24*	
Stokes Shift	0.6		0.6	
S_1-min	Directly to S_1-CI*		4.46 (0.16) *2.80*	
Stokes Shift			2.0	
S_1-min-asym		4.78 (0.35) *3.42*		4.64 (0.37) *3.41*
Stokes Shift		1.6		1.4

energy surface (PES). Further geometry optimization, starting from a slightly non-planar geometry, leads indeed directly to a crossing region with S_0. A structure belonging to this region, which we shall refer to as S_1-CI* (to highlight that we have not located the real CI), is shown in Figure 7b. S_1-CI* is characterized by a strong out-of-plane motion of the carbonyl group. The crossing region is reached without any crossing with another excited state (i.e. on the PES of the same diabatic state as in the FC region).

By using the larger 6-311 + G(2d,2p) basis set, a picture pretty similar to that just described was found. We find a planar stationary point, characterized by a Stokes Shift of only 0.5 eV, which is less stable than a non-planar minimum (S_1-min, see Figure S11 in the SI), exhibiting a strong pyramidalization of the carbonyl group, which is characterized by a very large Stokes Shift of (~2 eV) and low emission energy (2.8 eV). Indeed, S_1-min is isoenergetic with a crossing region with S_0, reached by further out-of-plane motion of the carbonyl group.

PCM/TD–M052X/6-31G(d) geometry optimizations of S_2 predict that a steep path leads to a crossing with S_1, and then two possible outcomes are predicted. Either the population is transferred on S_1 and then proceeds directly towards S_1-CI* (path a in Figure 9), or another minimum, also on the S_1 diabatic surface, is reached (path b in Figure 9). This minimum, which is

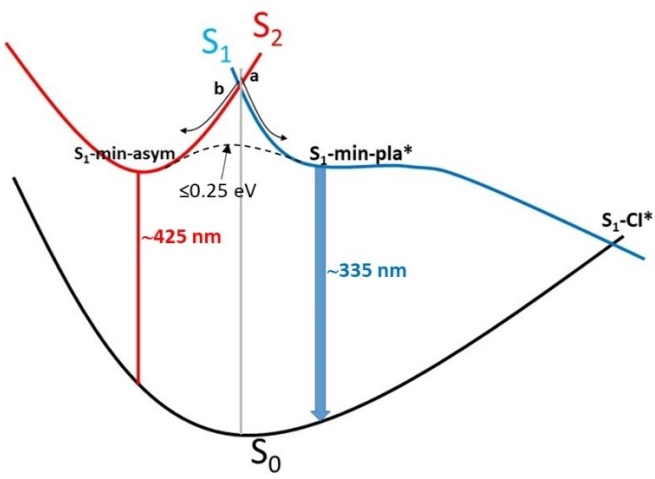

Figure 9. Schematic depiction of the main deactivation paths in εG, according to PCM/TD-M052X calculations.

0.1 eV less stable than S_1-min-pla*, is associated to the transition from the HOMO to a π* orbital mainly localized on the etheno ring (see Figure S12 in the SI), i.e. much more asymmetric with respect to the virtual orbital involved in the S_2 transition in the FC region (where the contribution of the imidazole ring to the MO is larger, see Figure S12). As a consequence, we label this minimum (depicted in Figure 7c) as S_1-min-asym. In this minimum, the etheno-ring is 'bent' with respect to the molecular plane, and the C2 atom (Figure 1) is quite significantly pyramidalized. The emission intensity is large (oscillator strength 0.37), as well as the Stokes Shift (~1.6 eV).

S_1-min-asym is located also by using the larger 6-311 + G(2d,2p) basis, it appears to be less stable than S_1-min-pla* by 0.14 eV, and it is strongly emissive, with a Stokes Shift of ~1.4 eV. As detailed in the SI, we have repeated this analysis also for εG, obtaining a picture similar to that obtained with explicit water molecules.

In Figure 8, we report also the computed vibrationally resolved emission spectrum, simulated in the hypothesis that the population of S_1-min-pla* and S_1-min-asym is the same. The computed spectrum is in remarkable agreement with the experimental steady-state fluorescence spectrum, with a less intense peak just below 300 nm and a broad band with a maximum of ~380 nm. These two peaks are slightly blue-shifted with respect to the experimental features, but the discrepancy is much smaller than what was expected based on the analysis of the emission energies, due to the proper inclusion of vibronic effects. It is important to notice that the relative intensity of the two peaks in the fluorescence spectrum will obviously depend on the population of the two associated minima (whose exact assessment would need a purposely devoted dynamical study). Based on the comparison with the experiments and considering the possible errors in the computed emission intensity, however, it seems that our working hypothesis (i.e. 50% of the population for the two minima) is reasonable.

Discussion

In this study, we have characterized the excited state decay of the mutagenic etheno adduct of 2'-deoxyguanosine εdG by integrating steady-state and time-resolved spectroscopy with

quantum mechanical calculations. The results show that etheno substitution has a large effect on the spectral properties of dG or dGMP.[40,41] As a first observation, the shapes of the fluorescence bands of εdG and dGMP are very different. While for dGMP it is dominated by a sharp peak around 334 nm accompanied by a long tail towards longer wavelengths, that of εdG is much broader and centered at 410 nm, with a broad shoulder at 350 nm (on the blue side), and a tail towards longer wavelengths. More importantly, we observe a significant increase in the lifetime, which is 10 times larger at longer wavelengths, and of the quantum yield, 6 times higher with respect to those measured for dG or dGMP (Table S1).[40,41] In addition, as shown in Table 5 below, the "average" lifetimes (see Equation (6)), used here as qualitative values, of εdG are significantly longer than those of dGMP. While the values are close in the blue edge (320 nm), where $<\tau>$ is about 0.5 ps for dGMP and 0.6 ps for εdG, they diverge strongly when moving towards longer wavelengths. Above 450 nm, $<\tau>$ is only about 1.4 ps for dGMP while it is more than 20 ps for εdG.

The spectral evolution of εdG is also remarkably different from that observed for dGMP. The fluorescence of dGMP corresponds to a single band rapidly red-shifting, this spectral red-shift being correlated with an increase of the width. Time-resolved fluorescence spectra of εdG are instead dominated at early times by a very strong peak around 335 nm, i.e with a very small Stokes Shift with respect to absorption. This peak disappears within a few hundred of femtoseconds, whereas the fluorescence on the ps timescale is dominated by a large band peaking at ~430 nm, and survives for much longer than the studied time interval of 10 ps. As explained above (and illustrated in Figure S9), deconvolution of the spectra suggests the involvement of two separate states. Also, the zero-time anisotropy of dGMP was substantially higher, about 0.2 at all wavelengths, than that of εdG, about 0.1 at all wavelengths. Interestingly, the fluorescence anisotropy close to zero-time is lower below 400 nm than above, as illustrated in Figure S8. Moreover, the fluorescence anisotropy above 400 nm increases slightly in time during the first picoseconds (Figure 4). Although the error associated with a very weak fluorescence signal does not allow an unambiguous conclusion, this behavior can be explained by the time-dependent superposition of two emissions: the "blue" band, having a slightly lower anisotropy, and the "red" band, having a slightly higher anisotropy. At time-zero, the "blue" band dominates the emission, but its rapid disappearance within a few picoseconds, as testified by the time-resolved fluorescence spectra, leads to the increase of the fluorescence anisotropy as observed at longer wavelengths.

Table 5. Average lifetimes (in ps) of εdG and dGMP at various wavelengths.

εdG		dGMP[a]	
λ (nm)	$<\tau>$	λ (nm)	$<\tau>$
320	0.63	310	0.52
340	3.76	330	0.68
360	3.63	360	0.74
380	7.55	420	1.11
420	18.16	450	1.36
440	22.98	500	1.67
460	21.95	600	2.29

[a] Calculated from data in reference.[40]

Our calculations, as depicted in Figure 8, provide a rationale for the peculiar behavior of εdG and for the differences with respect to dGMP.[38] In both compounds, we find two close-lying bright transitions in the lowest energy absorption band. In dGMP, the high-energy one (L_b) is significantly more intense than the low-energy one (L_a), whereas in εdG the intensities of the two lowest energy bright transitions are quite similar.

In the canonical nucleotide, experiments and calculations agree in predicting an ultrafast $L_b \rightarrow L_a$ population transfer (within 100 fs).[38,40] Then, the system passes through an energy plateau, where the purine ring keeps a geometry close to planarity, before reaching the crossing region with the S_0, by a barrierless out-of-plane motion of the C2-NH_2 moiety. This picture gives an account of the ultrafast decay and time-resolved spectra, which can be interpreted as a diffusion of the excited wave-packet on a relatively "flat" potential energy surface before reaching the S_1/S_0 conical intersection.

For εdG, we obtain a very different picture. Due to the presence of the etheno ring, the size of the conjugated π system increases, and S_1 and S_2 appear as strongly vibronically coupled transitions involving MO's delocalized over three rings (see Figure S10 in the SI). According to our calculations, in the first fs after 267 nm excitation (which populates nearly exclusively S_2), most of the S_2 population is transferred to S_1, and the system decays towards a planar stationary point, S_1-min-pla*, with small structural shifts with respect to the FC point, and, therefore, very small fluorescence Stokes Shift. The very intense band at ~335 nm dominating the time-resolved fluorescence spectra on the sub-ps time scale and appearing as a shoulder in the steady-state fluorescence spectra, should thus be associated to emission from S_1-min-pla*. The process [absorption on S_2] → [emission from S_1-min-pla*] is characterized by strongly negative anisotropy (see Table S2). Moreover, intramolecular vibrations can lead to significant mixing and transfer of intensity between these two transitions. On this ground, considering the contribution of the other emissive processes operative (see Table S2), we can understand why emission is characterized by very low zero-time anisotropy values at $\lambda < 400$ nm and only about 0.1 at $\lambda > 400$ nm. This experimental result confirms that a very efficient electronic relaxation takes place at a timescale well below the time-resolution of our equipment.

However, S_1-min-pla* is not a real minimum of the PES and the system can decay towards a crossing region with S_0, reached via an out-of-plane motion of the carbonyl group (this is another difference with respect to guanine).

On the other hand, and this is the most significant difference with respect to previous works on guanine,[38] our calculations suggest that for εdG part of the S_2 population

can decay to a minimum, S_1-min-asym, where the LUMO is mainly localized on the etheno ring. This minimum is strongly emissive, and its emission energy is consistent with the experimental maximum at ca. 425 nm. Even a small amount of population trapped on S_1-min-asym can give an account of the maximum in the steady state fluorescence spectrum. The process [absorption on S_2] → [emission from S_1-min-asym] is characterized by an anisotropy of 0.24 (see SI), in line with observations (Figure 4). As already mentioned above, the relative contribution of this process when measuring the fluorescence anisotropy at 440 nm (Figure 4) likely increases with time, providing a possible explanation for the small increases of the fluorescence anisotropy measured after 1 ps. Indeed, in the first ps, we can have a larger contribution from the emission associated with the path leading to S_1-CI*, which is expected to be associated with low anisotropy values. The molecular structure is strongly distorted with respect to the FC point and in the wave-packet there is the contribution of the population excited on S_2. Interestingly, a rather small energy barrier ($\leq$0.25 eV, see computational details and Figure 9) separates S_1-min-asym from S_1-min-pla*, suggesting that S_1-CI* could be provide a major non-radiative deactivation route for all the excited WP. The out-of-plane motion of the carbonyl group requires a quite substantial rearrangement of its solvation cage, which can delay the ground state recovery even in the absence of any substantial energy barrier. More importantly, part of the WP can be trapped in S_1-min-asym. These effects can explain why εdG exhibits a fluorescence quantum yield six times larger than that of dGMP. On the other hand, no real energy barrier separates S_1-min-CI* from the planar region, which is accessible (overcoming a small barrier) also from S_1-min-asym. On this ground, we can explain why the fluorescence quantum yield of εdG remains quite low $<$0.02.

It is interesting to compare the situation εdG/dGMP with that of εdC/dC (or dCMP).[13] In the latter case, our recent joint experimental and computational approach showed that the addition of an extra etheno ring on the canonical dC skeleton alters its photobehavior significantly. This structural change decreases the efficiency of the nonradiative deactivation of the emissive state, lengthening the excited state lifetime and increasing its emission quantum yield. Although the main nonradiative decay pathway to the ground state goes through an ethene-like conical intersection, the presence of a sizable energy barrier on the potential energy surface of the emissive ππ* state explains the increased fluorescence lifetimes with respect to that of dC. To first sight, etheno substitution has a similar effect on dG. We evidenced experimentally an increase in the singlet excited state lifetime and fluorescence quantum yields and assigned to emission from the lowest ππ* singlet state. But, on the other hand, as discussed above, the differences between εdG and dGMP are much more significant. There are indeed several qualitative differences in the anisotropy and in the spectral evolution that cannot be explained by a simple lengthening of the excited state lifetime, and suggest qualitative differences in their deactivation mechanism. As above mentioned, two separate emissive species are involved in the observed εdG relaxation process during the first 10 picoseconds (Figures 5 and 6): the shorter-lived emission, with a maximum centered at 335 nm, assigned to emission from the stationary point S_1-min-pla* and the longer-lived signal at 425 nm corresponding to the real minimum (S_1-min-asym*). Moreover, our calculations suggest that the excited states associated with these minima are strongly coupled and the two paths can communicate, giving an account of the peculiar time-resolved behavior. For C, a single bright excited state dominates the radiative dynamics, and etheno substitution 'simply' modulates the energy barrier towards the conical intersection, which occurs with the same mechanism of the parent nucleobase. For G, instead, two bright excited states are present in the lowest energy absorption band, and etheno substitution strongly affects their nature and interplay. εdG appears as a quite large, fairly symmetric, and stiff conjugated system, with three fused rings. In fact, according to our calculations, the preferred non-radiative path involves the carbonyl group. Shortly, from the electronic point of view, a fairly different system with respect to the parent G nucleobase.

Finally, it is worthwhile to discuss the implications of our results on the isolated εdG nucleoside for the photoactivated dynamics of DNA sequences where εdG substitutes its parent dG base. Though the inclusion of εdG in a polynucleotide chain is indeed expected to affect its photophysics (which is the case for dG), the substitution of a single nucleobase can significantly modulate the behavior of longer DNA sequences.[2,3,38,42–45] A first important effect is related to the substantial ($>$10 nm) redshift of the absorption spectrum of εdG with respect to that of dG (Table S1), indicating a larger absorption of εdG-containing sequences in the UVA region. This is important since the UVA component of solar radiation is not totally screened by the Earth's atmosphere. This is indeed what happens for the sequences containing 5-formylcytosine or 5-methylcytosine (5 mC), whose absorption spectrum is red-shifted with respect to that of cytosine.[9,45–51] Interestingly, this effect has been evoked to explain the larger mutagenicity of 5 mC-containing sequences following UVB irradiation.[45] Understanding what would be the consequences of the larger fluorescence quantum yield and excited state lifetime induced by etheno substitution of G in DNA sequences is less straightforward. On the one hand, there is general agreement on the existence of 'monomer-like' decay channels, i.e. associated with excited states localized on a single nucleobase, in oligonucleotides.[2,3,52] Using again 5 mC as a representative example, sequences with C→5 mC substitution exhibit a larger fluorescence quantum yield, mirroring the behavior of the isolated bases.[45] On the other hand, within duplexes a large part of the photoexcited population of dG bases is known to be transferred to excited states with significant Charge Transfer character,[3,9,53–55] which can also trigger inter-strand proton transfer.[3,56] These processes could be operative also for εdG, quenching its fluorescence. However, the characterization of the photoactivated behavior of εdG-containing DNA sequences is well beyond the scope of this study. Nonetheless, to get some preliminary insights on this issue, we have used the

same computational approach adopted for εdG to study two sequences where εdG is included in a duplex containing two or three bases, namely (dGpdC)(εdGpdC), hereafter labelled as GC·εdGC, and (dGpdCpdG)(dCεdGpdC), hereafter GCG·CεdGC (see Figure 10). As discussed in detail in Section "Including εdG within a duplex" of the SI, our calculations indicate that (i) the presence of εdG is expected to increase the structural disorder of a DNA duplex and (ii) *syn* conformation is favored, which allows a large exposure of the base to the solvent. Moreover, in the majority of the sequences examined the lowest energy excited state (S_1) in the FC region is well localized on the εdG base. This outcome represents a significant difference with respect to 'natural' GC sequences, where, by using the same level of calculation, the lowest energy excited states have a strong G→C CT character. The outcome of S_1 geometry optimizations for GC·εdGC and GCG·CεdGC is also consistent with that obtained for εdG, and both S_1-min-pla and S_1-min-asym minima, described for the free base, have been located within the duplex (see SI for details). Shortly, also considering that εdG should reduce the local stiffness of the duplex, many of the photophysical features we have described for the free base should also be relevant for the future study of εdG in DNA.

Another important property of dG-containing helices that could be affected by etheno substitution is the ionization potential. As discussed in the SI, the ionization potential of εdG is ~0.2 eV smaller than that of G. Considering that G is the base with the lowest ionization potential (and therefore more prone to be involved in several oxidative processes), this result suggests that εdG could act as an even more efficient sink for the 'electron hole' which can be formed in a DNA sequence either by direct UV absorption or following the interaction of 'external' oxidants.[42,57,58]

Conclusions

Our joint experimental and computational approach provides a comprehensive picture of the main effects governing the photophysics of 1,N^2-etheno-2′-deoxyguanosine (εdG). The presence of the extra etheno ring confers εdG a peculiar photobehavior compared to that of its canonical counterpart, with the presence of two separate emissions evidenced by fluorescence upconversion experiments. These emissions correspond to the presence of different minima on the S_1 surface, a stationary point S_1-min-pla* responsible for the short-lived signal peaking at 335 nm, and a more stable minimum, S_1-min-asym, accounting for the broadband at 425 nm. Indeed, the lengthening of εdG lifetime with respect to that of originally present dG might modify the high DNA resistance towards UV

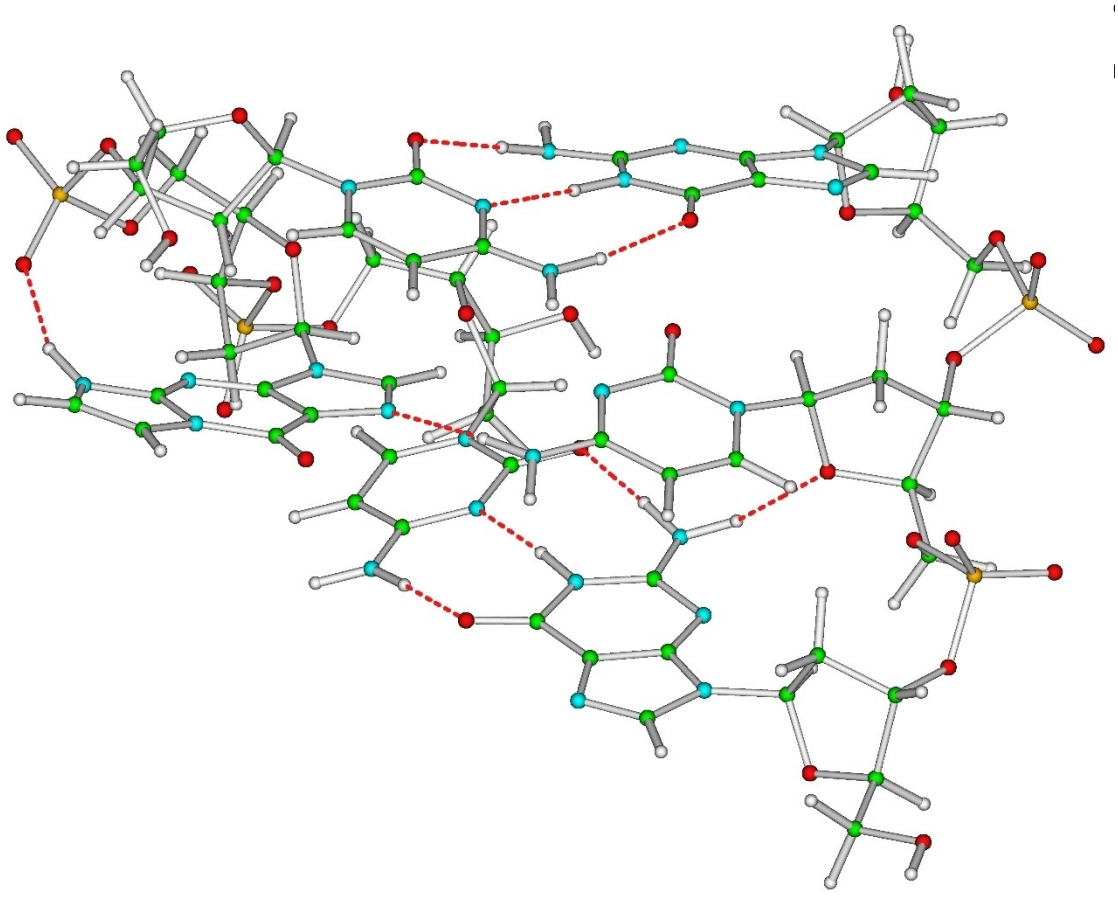

Figure 10. Schematic drawing of the GCG·CεGC, where εdG is in *syn* conformation.

light, slowing down the efficient non-radiative deactivation pathways.

Our computational analysis of short oligomers containing εdG shows that many of the photophysical features of εdG are also maintained in duplex, which suggests that this modified base could have a significant impact on the structural and photoactivated dynamics of DNA. In addition, the ionization potential of εdG is ~0.2 eV smaller than that of G, which makes the etheno derivative a better hole trap than the canonical base. This raises the question of whether the presence of εdG in a nucleic acid sequence could be a threat for the genome integrity not only in the dark, because of its established mutagenicity, but also under irradiation triggering undesired DNA photooxidation. Our combined experimental and computational study paves the route for future investigation on εdG-containing DNA sequences.

Experimental Section

Synthesis

3′,5′-O-bis(*tert*-butyldimethylsilyl)-2′-deoxyguanosine (1). Compound 1 was prepared from guanosine (8 g, 30 mmol) dissolved in anhydrous DMF (100 mL) under N_2 atmosphere. The solution was placed in an ice bath, then *tert*-butyldimethylsilyl chloride (TBDMSCl) (2 eq., 9 g, 60 mmol) and imidazole (4 g, 60 mmol) were added. The mixture stirred first for 10 min at 0 °C, and then overnight at room temperature under N_2 atmosphere. Finally, the reaction was quenched adding 100 mL of water, the precipitate was filtered, washed with water and dried under vacuum obtaining 1 as a white solid (11.9 g, 80%). ^{1}H NMR (300 MHz, DMSO-d6) δ 10.45 (s, 1H), 7.73 (s, 1H), 6.31 (s, 2H), 5.97 (m, 1H), 4.35 (m, 1H), 3.74–3.66 (m, 1H), 3.64–3.48 (m, 2H), 2.6–2.10 (m, 2H), 0.78–0.71 (s + s, 18H), −0.09 (s + s, 12H). ^{13}C NMR (75 MHz, DMSO-d6) δ 156.6, 153.6, 150.9, 134.8, 116.6, 86.9, 82.1, 72.1, 62.7, 25.7, 25.6, 17.8, 17.6, −4.8, −5.0, −5.5, −5.6. 3′,5′-O-bis(*tert*-butyldimethylsilyl)-1,N^2-Etheno-2′-deoxyguanosine (2). A DMF solution of 3′,5′-O-bis(*tert*-butyldimethylsilyl)-2′-deoxyguanosine (1) (4 g, 8.1 mmol) and K_2CO_3 (1.45 g, 10.5 mmol) in (40 mL) was stirred at room temperature for 10 min. Then, chloroacetaldehyde solution (50 wt% in H_2O, 1.43 mL, 11.3 mmol) was added dropwise, and the mixture was heated at 35 °C under nitrogen. Progress of the reaction was monitored using UV absorption spectrometry, and the reaction was stopped after 16 hours when the same absorption was reached at 272 and 254 nm. The reaction was quenched with 100 mL of water, the precipitate was filtered, washed with water and dried under vacuum. The resulting yellow solid was purified by column chromatography on silica gel using CH_2Cl_2: ethyl acetate (from 1:1 to 1:3, v:v) to afford 2 as a white solid (1 g, 25%). ^{1}H NMR (300 MHz, Chloroform-d) δ 8.42 (s, 1H), 7.61 (d, J = 2.5 Hz, 1H), 7.35 (d, J = 2.5 Hz, 1H), 6.38 (m, 1H), 4.60 (m, 1H), 4.10 (m, 1H), 3.86–3.73 (m, 2H), 2.55 (s, 2H), 0.98–0.79 (m, 18H), 0.18–0.00 (m, 12H). ^{13}C NMR (75 MHz, Chloroform-d) δ 150.9, 149, 146.3, 136.1, 116.6, 107.6, 88.7, 84.8, 72.5, 63.2, 41.1, 26.1, 25.9, 18.5, 18.2, −4.4, −4.6, −5.2, −5.3.

1,N^2-Etheno-2′-deoxyguanosine (εdG). In a plastic tube placed in an ice bath, a solution of HF/pyridine (70%, 456 mL) was added to 3′,5′-O-bis(*tert*-butyldimethylsilyl)-1,N^2-etheno-2′-deoxyguanosine (2) (400 mg, 0.77 mmol) dissolved in 4 mL pyridine. The ice bath was withdrawn, and the mixture was stirred at room temperature for 2 h. The solution was neutralized with 2 g of $NaHCO_3$, filtered and the solvent was removed by air stream. The residue was then purified by column chromatography on silica gel (CH_2Cl_2:MeOH, 19:1 to 5:1) to afford εdG as a white solid (63.7 mg, 29%). ^{1}H NMR (300 MHz, DMSO-d6) δ 8.13 (s, 1H), 7.60 (d, J = 2.7 Hz, 1H), 7.42 (d, J = 2.7 Hz, 1H), 6.26 (dd, J = 7.6, 6.0 Hz, 1H), 5.38–5.26 (m, 1H), 4.99 (m, 1H), 4.43–4.32 (m, 1H), 3.84 (m, 1H), 3.55 (m, 2H), 2.67–2.54 (m, 1H), 2.32–2.19 (m, 1H). ^{13}C NMR (75 MHz, DMSO-d6) δ 151.3, 149.9, 145.9, 136.9, 116.6, 115.3, 106.8, 87.6, 82.9, 70.7, 61.6. HRMS (ESI): calc for $C_{12}H_{13}N_5O_4$ $[M+H]^+$ 292.1046, found 292.1039.

UV-Vis Absorption

All UV-Vis absorption spectra were registered with a single beam Varian Cary 60 spectrophotometer, using quartz cells of 1 cm optical path length.

Steady-State Fluorescence

Spectra were measured upon 267 (255 or 300) nm excitation with a Fluorolog-3 (Horiba, Jobin-Yvon) fluorimeter. Solutions of εdG or TMP (used as standard) in PBS (0.1 M, pH 7.4) with an absorbance of 0.1 at the excitation wavelength were prepared. As the emissions of the neat buffered solutions were not negligible compared to that of εdG, they were recorded separately and subtracted from the spectra of the sample to remove their contribution. Moreover, the recorded spectra were corrected for the response of the detection system. Quantum yield was determined using thymidine monophosphate as reference ($\phi_F = 1.54\times10^{-4}$).[41]

Fluorescence Up Conversion Measurements

A detailed description of the femtosecond fluorescence upconversion equipment has been given earlier.[40] Briefly, the 267 nm excitation was generated as the third harmonic of a femtosecond mode-locked Ti-sapphire laser (Coherent MIRA 900, 800 nm, 76 MHz, 120 fs, 2 W average power). The average excitation power in the UV was set to 50 mW. The εdG solution (30 mL, OD = 0.5 in 1 mm at 267 nm) was flowing while the cell was continuously moving in order to avoid local degradation.

The fluorescence was collected and passed through a cutoff filter (WG305 orWG320) in order to eliminate the weak remaining UV excitation light and finally focused into a 1 mm BBO type I crystal using two off-axes parabolic mirrors collinearly with the IR gating beam. After the mixing of the fluorescence and the IR gating pulse in the NL crystal, the generated sum-frequency light was collected and focused on the entrance slit of a double monochromator equipped with a UV-sensitive photomultiplier (Hamamatsu 1527 P) connected to a photon counter (Stanford SR400).

Fluorescence decays were recorded at selected wavelengths with parallel (I_{par}(t)) or perpendicular (I_{perp}(t)) excitation/detection configurations. These were realized by controlling the polarization of the exciting beam with a zero-order half wave plate. The temporal scans were repeated several times and then averaged in order to improve the statistics.

For visualization, total fluorescence decay kinetics (F(*t*)) and fluorescence anisotropies R(*t*) were constructed[59] from the parallel and perpendicular signals according to the equation:

$$F(t) = I_{par}(t) + 2\, I_{perp}(t) \quad (1)$$

$$R(t) = (I_{par}(t) - I_{perp}(t))/F(t) \quad (2)$$

For the data treatment, parallel and perpendicular scans were treated together in a merged nonlinear fitting/deconvolution process using the impulse response model functions *i*(t) convoluted by the instrument response function *g*(*t*)

$$I'_{par}(t) = i_{par}(t) \otimes g(t) \quad (3a)$$

$$I'_{perp}(t) = i_{perp}(t) \otimes g(t) \quad (3b)$$

where the two impulse response model functions are given by

$$i_{par}(t) = (1 + 2r(t))f(t) \quad (4a)$$

$$i_{perp}(t) = (1 - r(t))f(t) \quad (4b)$$

f(t) and r(t) being the model functions representing the total fluorescence and the fluorescence anisotropy. The instrument response function g(t) was described by a simple Gaussian function

$$g(t) = e^{-0.5 \cdot (t/\sigma)^2} \quad (5)$$

The fwhm value of the Gaussian irf was kept free-floating but converged for all wavelengths to a value of about 400 fs.

The model functions I'_{par} and I'_{perp} thus obtained were fitted to the experimental parallel (I_{par}) and perpendicular (I_{perp}) signals. A simple biexponential function was used for *f*(t) for wavelengths below 400 nm, while an additional constant term was needed for longer wavelengths. The fluorescence anisotropy *r*(t) was described as mono- or bi-exponential functions, with or without a rise, depending on the wavelength (see the main text for details). Initial free-floating fits of the traces >400 nm were used to obtain "average" values for the rise, 3.7 ps, and the decay, 21 ps, of the fluorescence anisotropy. Final fits were then performed keeping these values fixed. For the traces <400 nm, no rise could be observed and only the decay was fixed.

In order to make an "easy" comparison of the non-exponential fluorescence decays we calculate the average lifetimes $<\tau>$ using the equation:[60]

$$\langle\tau\rangle = \frac{a_1\tau_1^2 + a_2\tau_2^2}{a_1\tau_1 + a_2\tau_2} \quad (6)$$

This "average lifetime" $<\tau>$ should be taken as just a qualitative measure without any real physical meaning.

Time-resolved fluorescence spectra were recorded at magic angle between 320 and 470 nm by scanning the monochromator with a step of 5 nm. Unfortunately, the detection system is blind around 400 nm due to scattered excitation light, so the spectra were recorded in two sequential regions 310–390 nm and 410–470 nm. 10 time-resolved spectra equally spaced by 1 ps were recorded over a 10 ps time window. The full wavelength – time sampling was repeated several times and then averaged in order to improve the statistics.

Resulting spectra were corrected with regards to the spectral sensitivity of the system using a phenomenological correction curve obtained by comparing a reference FU spectrum to the corresponding steady-state spectrum. For this purpose, the relaxed long-time spectrum (>200 ps) of the dye molecule DMQ in cyclohexane solution was used.

Computational Details

Our reference electronic methods have been DFT and its Time Dependent extension, TD-DFT. As functional, we choose M052X,[61] which have been already profitably used in the study of many (natural and modified) nucleobases and oligonucleotides.[2,3] Geometry optimizations and vibrational analysis have been performed with the cost-effective 6-31G(d) basis set, complemented by single point calculations with the larger 6-31+G(d,p) and 6-311+G(2d,2p) basis set, since the computed spectra are relatively more sensitive to the size of the basis set than the optimized geometry. Linear Interpolation Cartesian Coordinate calculations were done to estimate the upper limit of the barrier between S_1-min-asym and S_1-min-pla* at the PCM/M052X/6-31G(d).

Bulk solvent effects are included with the polarizable continuum (PCM)[62] model, whereas the effect of solute-solvent hydrogen bond interactions considered by adding three H_2O molecules to the computational model, with the arrangement shown in Figure 7 (which saturates the most important hydrogen bonding/acceptor groups in εG). This approach has been shown to provide a reliable description of solvent effects for many other nucleobases in water. Calculations have been also performed without including explicit water molecules.

All the TD-DFT calculations have been carried out with the Gaussian16 program.[63]

Vibrationally resolved spectra have been computed by using the FC*Classes3*[64] program. In detailed, we computed the frequencies for the ground and first four excited states at FC (S_0-S_4 for the absorption) and for the S_1 at the two minima (for emission) within the time dependent method and the vertical hessian model. Then, each state has been broadened with a gaussian with half-width half-maximum = 0.05 eV.

CASPT2. The absorption spectrum and PES in the gas phase have also been computed using the CASPT2/CASSCF[65,66,67] protocol with an (18,14) active space and using OpenMolcas.[68] See SI for further details.

Acknowledgements

The research leading to these results has received funding from LASERLAB-EUROPE (grant agreement no. 654148, European Union's Horizon 2020 research and innovation programme), and from the Spanish (project PID2021-128348NB-I00 and Severo Ochoa Center of Excellence Program CEX2021-001230-S funded by MCIN/AEI/10.13039/501100011033/ and "FEDER a way of making Europe") and regional (CIAICO/2021/061) governments. RI thanks the CNR program "Progetti di Ricerca @cnr'', project UCATG4, NUTRAGE funded by FOE-2021 DBA.AD005.225, and CN3, National Center for GeneTherapy and Drugs based on RNA technology, funded by the European Union-NextGenerationEU-PNRR, for financial support.

Conflict of Interests

The authors declare no conflict of interest.

Data Availability Statement

The data that support the findings of this study are available from the corresponding author upon reasonable request.

Keywords: DNA damage · Computational chemistry · Excited state dynamics · Femtosecond spectroscopy · Fluorescence upconversion · Internal conversion · Ultrafast non-radiative processes

[1] *DNA Photodamage. From Light Absorption to Cellular Response and Skin Cancer*, (Eds: R. Improta, T. Douki), Royal Society Of Chemistry, Cambridge, **2021**.
[2] R. Improta, F. Santoro, L. Blancafort, *Chem. Rev.* **2016**, *116*, 3540–3593.
[3] L. Martínez Fernández, F. Santoro, R. Improta, *Acc. Chem. Res.* **2022**, *55*, 2077–2087.
[4] T. Gustavsson, D. Markovitsi, *Acc. Chem. Res.* **2021**, *54*, 1226–1235.
[5] W. J. Schreier, P. Gilch, W. Zinth, *Annu. Rev. Phys. Chem.* **2015**, *66*, 497–519.
[6] S. Boldissar, M. S. de Vries, *Phys. Chem. Chem. Phys.* **2018**, *20*, 9701–9716.
[7] R. Brem, P. Karran, *Photochem. Photobiol.* **2012**, *88*, 5–13.
[8] B. Ashwood, M. Pollum, C. E. Crespo-Hernández, *Photochem. Photobiol.* **2019**, *95*, 33–58.
[9] L. Esposito, A. Banyasz, T. Douki, M. Perron, D. Markovitsi, R. Improta, *J. Am. Chem. Soc.* **2014**, *136*, 10838–10841.
[10] A. M. Fleming, C. J. Burrows, *Org. Biomol. Chem.* **2017**, *15*, 8341–8353.
[11] V. Vendrell-Criado, G. M. Rodriguez-Muniz, M. C. Cuquerella, V. Lhiaubet-Vallet, M. A. Miranda, *Angew. Chem. Int. Ed.* **2013**, *52*, 6476–6479.
[12] M. Lineros-Rosa, A. Frances-Monerris, A. Monari, M. A. Miranda, V. Lhiaubet-Vallet, *Phys. Chem. Chem. Phys.* **2020**, *22*, 25661–25668.
[13] P. Lizondo-Aranda, L. Martínez-Fernández, M. A. Miranda, R. Improta, T. Gustavsson, V. Lhiaubet-Vallet, *J. Phys. Chem. Lett.* **2022**, *13*, 251–257.
[14] R. C. Fernando, J. Nair, A. Barbin, J. A. Miller, H. Bartsch, *Carcinogenesis* **1996**, *17*, 1711–1718.
[15] F.-L. Chung, H.-J. C. Chen, R. G. Nath, *Carcinogenesis* **1996**, *17*, 2105–2111.
[16] Y. Yu, Y. Cui, L. J. Niedernhofer, Y. Wang, *Chem. Res. Toxicol.* **2016**, *29*, 2008–2039.
[17] C. C. M. Garcia, J. P. F. Angeli, F. P. Freitas, O. F. Gomes, T. F. de Oliveira, A. P. M. Loureiro, P. Di Mascio, M. H. G. Medeiros, *J. Am. Chem. Soc.* **2011**, *133*, 9140–9143.
[18] Y. Yu, C. R. Guerrero, S. Liu, N. J. Amato, Y. Sharma, S. Gupta, Y. Wang, *Mol. Cell. Proteomics* **2016**, *15*, 810–817.
[19] A. K. Basu, M. L. Wood, L. J. Niedernhofer, L. A. Ramos, J. M. Essigmann, *Biochemistry* **1993**, *32*, 12793–12801.
[20] A. Barbin, H. Bartsch, P. Leconte, M. Radman, *Nucleic Acids Res.* **1981**, *9*, 375–387.
[21] U. Fedeli, P. Girardi, G. Mastrangelo, *World J Gastroenterol.* **2019**, *25*, 4885–4891.
[22] C. C. M. Garcia, F. P. Freitas, P. Di Mascio, M. H. G. Medeiros, *Chem. Res. Toxicol.* **2010**, *23*, 1245–12545.
[23] A. Barbin, H. Ohgaki, J. Nakamura, M. Kurrer, P. Kleihues, J. A. Swenberg, *Cancer Epidemiol. Biomarkers Prev.* **2003**, *12*, 1241–1247.
[24] F. El Ghissassi, A. Barbin, J. Nair, H. Bartsch, *Chem. Res. Toxicol* **1995**, *8*, 278–283.
[25] B. Tudek, D. Zdżalik-Bielecka, A. Tudek, K. Kosicki, A. Fabisiewicz, E. Speina, *Free Radic. Biol. Med.* **2017**, *107*, 77–89.
[26] S. S. Hecht, *Chem. Res. Toxicol.* **2017**, *30*, 367–375.
[27] H. Chen, S. Krishnamachari, J. Guo, L. Yao, P. Murugan, C. J. Weight, R. J. Turesky, *Chem. Res. Toxicol.* **2019**, *32*, 1850–1862.
[28] I. Ohnishi, Y. Iwashita, Y. Matsushita, S. Ohtsuka, T. Yamashita, K. Inaba, A. Fukazawa, H. Ochiai, K. Matsumoto, N. Kurono, Y. Matsushima, H. Mori, S. Suzuki, S. Suzuki, F. Tanioka, H. Sugimura, *Genes Environ.* **2021**, *43*, 12.
[29] K. V. Petrova, R. S. Jalluri, I. D. Kozekov, C. J. Rizzo, *Chem. Res. Toxicol.* **2007**, *20*, 1685–1692.
[30] T. Obtułowicz, A. Winczura, E. Speina, M. Swoboda, J. Janik, B. Janowska, J. M. Cieśla, P. Kowalczyk, A. Jawien, D. Gackowski, Z. Banaszkiewicz, I. Krasnodebski, A. Chaber, R. Olinski, J. Nair, H. Bartsch, T. Douki, J. Cadet, B. Tudek, *Free Radic. Biol. Med.* **2010**, *49*, 1064–1071.
[31] S. Akasaka, F. P. Guengerich, *Chem. Res. Toxicol.* **1999**, *12*, 501–507.
[32] S. Langouët, A. N. Mican, M. Müller, S. P. Fink, L. J. Marnett, S. A. Muhle, F. P. Guengerich, *Biochemistry* **1998**, *37*, 5184–5193.
[33] H. Zang, A. K. Goodenough, J.-Y. Choi, A. Irimia, L. V. Loukachevitch, I. D. Kozekov, K. C. Angel, C. J. Rizzo, M. Egli, F. P. Guengerich, *J. Biol. Chem.* **2005**, *280*, 29750–29764.
[34] H. Ling, F. Boudsocq, R. Woodgate, W. Yang, *Cell* **2001**, *107*, 91–102.
[35] G. Shanmugam, A. K. Goodenough, I. D. Kozekov, F. P. Guengerich, C. J. Rizzo, M. P. Stone, *Chem. Res. Toxicol.* **2007**, *20*, 1601–1611.
[36] P. D. Sattsangi, N. J. Leonard, C. R. Frihart, *J. Org. Chem.* **1977**, *42*, 3292–3296.
[37] J. T. Kusmierekt, B. Singer, *Chem. Res. Toxicol.* **1992**, *5*, 634–638.
[38] V. Karunakaran, K. Kleinermanns, R. Improta, S. A. Kovalenko, *J. Am. Chem. Soc.* **2009**, *131*, 5839–5850.
[39] F. J. Avila Ferrer, J. Cerezo, E. Stendardo, R. Improta, F. Santoro, *J. Chem. Theory Comput.* **2013**, *9*, 2072–2082.
[40] F. A. Miannay, T. Gustavsson, A. Banyasz, D. Markovitsi, *J. Phys. Chem. A* **2010**, *114*, 3256–3263.
[41] D. Onidas, D. Markovitsi, S. Marguet, A. Sharonov, T. Gustavsson, *J. Phys. Chem. B* **2002**, *106*, 11367–11374.
[42] I. Saito, T. Nakamura, K. Nakatani, Y. Yoshioka, K. Yamaguchi, H. Sugiyama, *J. Am. Chem. Soc.* **1998**, *120*, 12686–12687.
[43] E. Meggers, M. E. Michel-Beyerle, B. Giese, *J. Am. Chem. Soc.* **1998**, *120*, 12950–12955.
[44] E. Balanikas, A. Banyasz, T. Douki, G. Baldacchino, D. Markovitsi, *Acc. Chem. Res.* **2020**, *53*, 1511–1519.
[45] L. Martinez-Fernandez, A. Banyasz, L. Esposito, D. Markovitsi, R. Improta, *Signal Transduct. Target. Ther.* **2017**, *2*, 17021.
[46] A. Francés-Monerris, M. Lineros-Rosa, M. A. Miranda, V. Lhiaubet-Vallet, A. Monari, *Chem. Commun.* **2020**, *56*, 4404–4407.
[47] P. Kabaciński, M. Romanelli, E. Ponkkonen, V. K. Jaiswal, T. Carell, M. Garavelli, G. Cerullo, I. Conti, *J. Phys. Chem. Lett.* **2021**, *12*, 11070–11077.
[48] X. Wang, L. Martínez-Fernández, Y. Zhang, P. Wu, B. Kohler, R. Improta, J. Chen, *J. Am. Chem. Soc.* **2024**, *146*, 1839–1848.
[49] X. Wang, L. Martínez-Fernández, Y. Zhang, K. Zhang, R. Improta, B. Kohler, J. Xu, J. Chen, *Chem. Eur. J.* **2021**, *27*, 10932–10940.
[50] L. Martínez-Fernández, A. J. Pepino, J. Segarra-Martí, A. Banyasz, M. Garavelli, R. Improta, *J. Chem. Theory Comput.* **2016**, *12*, 4430–4439.
[51] L. Martínez-Fernández, A. J. Pepino, J. Segarra-Martí, J. Jovaišaitei, I. Vaya, A. Nenov, D. Markovitsi, T. Gustavsson, A. Banyasz, M. Garavelli, R. Improta, *J. Am. Chem. Soc.* **2017**, *139*, 7780–7791.
[52] *Photoinduced Phenomena in Nucleic Acids II–DNA Fragments and Phenomenological Aspects* (Eds: M. Barbatti, A. C. Borin, S. Ullrich) Springer, Cham, **2015**.
[53] J. A. Green, S. Gómez, G. Worth, F. Santoro, R. Improta, *Chem. Eur. J.* **2022**, *28*, e202201731.
[54] J. A. Green, M. Yaghoubi Jouybari, H. Asha, F. Santoro, R. Improta, *J. Chem. Theory Comput.* **2021**, *17*, 4660–4674.
[55] H. Asha, J. A. Green, L. Esposito, L. Martinez-Fernandez, F. Santoro, R. Improta, *J. Phys. Chem. B* **2022**, *126*, 10608–10621.
[56] L. Martinez-Fernandez, R. Improta, *Faraday Discuss.* **2018**, *207*, 199–216.
[57] A. Kumar, M. D. Sevilla, *Chem. Rev.* **2010**, *110*, 7002–7023.
[58] J. Cadet, T. Douki, J.-L. Ravanat, *Acc. Chem. Res.* **2008**, *41*, 1075–1083.
[59] T. Gustavsson, Á. Bányász, E. Lazzarotto, D. Markovitsi, G. Scalmani, M. J. Frisch, V. Barone, R. Improta, *J. Am. Chem. Soc.* **2006**, *128*, 607–619.
[60] A. Sillen, Y. Engelborghs, *Photochem. Photobiol.* **1998**, *67*, 475–486.
[61] Y. Zhao, N. E. Schultz, D. G. Truhlar, *J. Chem. Theory and Comput.* **2006**, *2*, 364–82. DOI: 10.1021/ct0502763.
[62] J. Tomasi, B. Mennucci, R. Cammi, *Chem. Rev.* **2005**, *105*, 2999–3093. DOI: 10.1021/cr9904009.
[63] Gaussian 16, Revision C.01, M. J. Frisch, G. W. Trucks, H. B. Schlegel, G. E. Scuseria, M. A. Robb, J. R. Cheeseman, G. Scalmani, V. Barone, G. A. Petersson, H. Nakatsuji, X. Li, M. Caricato, A. V. Marenich, J. Bloino, B. G. Janesko, R. Gomperts, B. Mennucci, H. P. Hratchian, J. V. Ortiz, A. F. Izmaylov, J. L. Sonnenberg, D. Williams-Young, F. Ding, F. Lipparini, F. Egidi, J. Goings, B. Peng, A. Petrone, T. Henderson, D. Ranasinghe, V. G. Zakrzewski, J. Gao, N. Rega, G. Zheng, W. Liang, M. Hada, M. Ehara, K. Toyota, R. Fukuda, J. Hasegawa, M. Ishida, T. Nakajima, Y. Honda, O. Kitao, H. Nakai, T. Vreven, K. Throssell, J. A. Montgomery, Jr., J. E. Peralta, F. Ogliaro, M. J. Bearpark, J. J. Heyd, E. N. Brothers, K. N. Kudin, V. N. Staroverov, T. A. Keith, R. Kobayashi, J. Normand, K. Raghavachari, A. P. Rendell, J. C. Burant, S. S. Iyengar,

J. Tomasi, M. Cossi, J. M. Millam, M. Klene, C. Adamo, R. Cammi, J. W. Ochterski, R. L. Martin, K. Morokuma, O. Farkas, J. B. Foresman, D. J. Fox, Gaussian, Inc., Wallingford CT, **2016**.
[64] FCclasses3: Vibrationally-resolved spectra simulated at the edge of the harmonic approximation Javier Cerezo, Fabrizio Santoro First published: 15 November 2022, https://doi.org/10.1002/jcc.27027.
[65] K. Andersson, P. A. Malmqvist, B. O. Roos, A. J. Sadlej, K. Wolinski, *J. Phys. Chem.* **1990**, *94*, 5483–5488.
[66] K. Andersson, P. Malmqvist, B. O. Roos, *J.Chem. Phys.* **1992**, *96*, 1218–1226.
[67] J. Finley, *Chem. Phys. Lett* **1998**, *288*, 299–306
[68] I. Fdez. Galván, M. Vacher, A. Alavi, C. Angeli, F. Aquilante, J. Autschbach, J. J. Bao, S. I. Bokarev, N. A. Bogdanov, R. K. Carlson, *J. Chem. Theory Comput.* **2019**, *15*, 5925–5964.

Manuscript received: May 10, 2024
Accepted manuscript online: June 13, 2024
Version of record online: July 31, 2024